

Multiscale Microtubule Dynamics in Active Nematics

Linnea M. Lemma^{1,2}, Michael M. Norton,¹ Alexandra M. Tayar,² Stephen J. DeCamp¹, S. Ali Aghvami¹,
Seth Fraden,¹ Michael F. Hagan,¹ and Zvonimir Dogic^{2,1,*}

¹Department of Physics, Brandeis University, Waltham, Massachusetts 02453, USA

²Department of Physics, University of California at Santa Barbara, Santa Barbara, California 93106, USA

(Received 27 June 2020; revised 14 June 2021; accepted 12 August 2021; published 27 September 2021)

In microtubule-based active nematics, motor-driven extensile motion of microtubule bundles powers chaotic large-scale dynamics. We quantify the interfilament sliding motion both in isolated bundles and in a dense active nematic. The extension speed of an isolated microtubule pair is comparable to the molecular motor stepping speed. In contrast, the net extension in dense 2D active nematics is significantly slower; the interfilament sliding speeds are widely distributed about the average and the filaments exhibit both contractile and extensile relative motion. These measurements highlight the challenge of connecting the extension rate of isolated bundles to the multimotor and multifilament interactions present in a dense 2D active nematic. They also provide quantitative data that is essential for building multiscale models.

DOI: 10.1103/PhysRevLett.127.148001

Driven by the continuous injection of energy through the motion of microscopic constituents, active nematics exhibit chaotic flows that are tightly coupled to the continuous creation and annihilation of motile topological defects [1–5]. Such dynamics are described by continuum models in which the activity is introduced through a phenomenological active stress [6–11]. Experimental work characterized the large-scale nonequilibrium dynamics of active nematics [12–16]. In comparison, little is known about how the microscopic constituents determine the coarse-grained dynamics, especially for cytoskeletal active nematics [17,18]. For instance, while active stress is the defining feature of active nematics, predicting its magnitude or sign in terms of microscopic dynamics remains a significant challenge [19–23].

Single-molecule experiments elucidated the dependence of the kinesin stepping speed on both the magnitude and the direction of the load force it experiences [24–28]. Consequently, determining the motor load and speed in active nematics is important for informing the microscopic models. However, measuring the relative speed of a motor with the respect to the filament it is stepping along is not possible in dense active nematics. In the absence of such data, the relative motion of filaments provides valuable insight into microscopic dynamics. For example, several models predict that filaments will slide past each other at a constant speed determined by the molecular motors [18,29–32]. To test these predictions, we characterize the multiscale dynamics of microtubule-based active nematics. We find that dilute microtubule pairs extend at a constant speed, similar to the stepping dynamics of an isolated motor. In contrast to both the dilute bundles and theoretical predictions, the motion of microtubules in a dense nematic is more complex. The filament extension rate is both

significantly slower and more widely distributed about the average when compared to the dynamics of isolated bundles. These effects must be accounted for to develop accurate multiscale models that predict the chaotic dynamics of active nematics from the properties of the microscopic constituents.

Extensile microtubule bundles are an essential building block of diverse active matter systems [33–37], yet their dynamics have not been quantified. We adsorbed dilute microtubules onto a surfactant stabilized oil-water interface in the presence of kinesin motor clusters, a depletion agent, and an ATP regeneration system [Fig. 1(a)]. When two microtubules bundled together, the kinesin clusters linked adjacent filaments and moved toward their plus ends. For pairs with opposite polarity, motors stepping generated bundle extension [Fig. 1(b), Supplemental Material [38], Fig. S1]. Notably, the bundle length increased linearly with

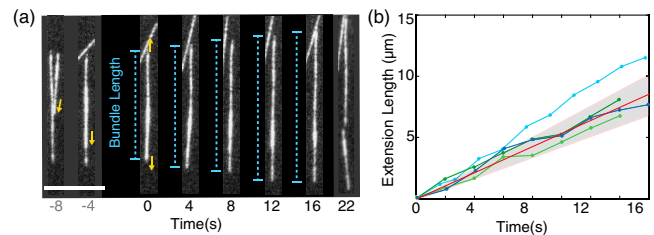


FIG. 1. Dynamics of extensile bundles. (a) Time series of two oppositely polarized microtubules cross-linked by kinesin motor clusters. Depletion induces bundle formation at $t = 0$ s. Thereafter, kinesin clusters generate bundle extension. Scale bar, $10 \mu\text{m}$. (b) Bundle length over time for four representative events. The red line indicates the average velocity of eight events, with shaded standard deviation. Average extension velocity $v = 540 \pm 100$ nm/s.

time, allowing us to extract the extension speed from the slope. The average extension speed was $\langle v_e \rangle = 540 \pm 100$ nm/s. For comparison, a single kinesin-1 motor steps with an average speed of $\langle v \rangle = 610 \pm 160$ nm/s [44], which extrapolates to a bundle extension speed of $1.2 \mu\text{m/s}$. This discrepancy can have different causes. For example, the crowding agent or cluster structure could change the angle and the force load with which motors attach to microtubules [28]. Diffusional dynamics suggest that the frictional force of interfilament sliding is 10^{-1} pN (see Supplemental Material [38]). This is large compared to the 10^{-5} pN drag force on a 100 nm bead, but small when compared to the 5 pN force at which kinesin motors stall [26,33,45].

The extensional bundle motion drives the large-scale dynamics of active nematics. To relate the two phenomena, we next measured the dynamics of microtubules in dense active nematics. Sedimenting a high density of extensile bundles onto a surfactant stabilized oil-water interface yielded an active nematic with local orientational order that was imaged using fluorescence microscopy. Nematic regions were labeled by photobleaching a $\sim 50 \mu\text{m}^2$ square in a defect-free, uniformly aligned region. Controls confirmed that the laser did not ablate the bleached microtubules. The bleached area remained constant over time, consistent with 2D incompressible flows (Supplemental Material [38], Fig. S2). The labeled nematic stretched along the director and compressed perpendicular to the director [Fig. 2(a), Supplemental Material [38], movie 1]. Occasionally, the rotational component of the strain dominated, causing the region to shear (Supplemental Material [38], Fig. S3). Our analysis excluded such regions.

We defined the x direction as the local nematic director in the Lagrangian reference frame. We first measured the intensity profile perpendicular to the director, $I_{\perp}(y)$ averaged across an edge of the photobleached region [Fig. 2(b)]. The interface remained sharp while the width of the bleached region decayed exponentially as $w = ae^{-t/\tau}$, where $\gamma_{\perp} = 1/\tau$ is the strain rate of the compressing material [Fig. 2(c)]. The ATP dependent strain rate was described by the Michaelis-Menten equation, the same relationship also describing the ATP-dependent stepping of an isolated motor [Fig. 2(g)] [26].

Next, we measured the average intensity profiles along the director $I_{\parallel}(x)$ averaged across the height of the bleached region. In contrast to the sharp edges perpendicular to the director, the edges along the director roughened [Fig. 2(d)]. Over time, the average edge intensity broadened in a diffusion-like manner [Fig. 2(e)]. We modeled the temporal evolution of such intensity profiles as a mass transfer process with diffusion and convection: $(\partial I_{\parallel}/\partial t) + \mathbf{u} \cdot \nabla I_{\parallel} = D_{\text{bleach}} \nabla^2 I_{\parallel}$, where \mathbf{u} is the velocity field and D_{bleach} is the activity-induced effective diffusion coefficient. Restricting the flows to be dipolar extensile and incompressible gives: $\mathbf{u} = \gamma_{\parallel} \{x, -y\}$, where γ_{\parallel} is the

constant strain rate. Assuming that gradients in the y direction are negligible yields

$$\frac{\partial I_{\parallel}}{\partial t} + x\gamma_{\parallel} \frac{\partial I_{\parallel}}{\partial x} = D_{\text{bleach}} \frac{\partial^2 I_{\parallel}}{\partial x^2}, \quad (1)$$

which we solved numerically. The strain rate and effective diffusion coefficients were obtained by minimizing the squared error between experimental intensity profiles and model predictions. The predicted intensity profiles quantitatively described the data [Fig. 2(e)], yielding the ATP-dependent effective diffusion D_{bleach} and γ_{\parallel} [Fig. 2(f)]. Importantly, the measured strain rates were comparable to those extracted from the perpendicular intensity profiles, $I_{\perp}(y)$ [Fig. 2(g)].

Photobleaching revealed the average dipolar extensile flows. Along the extension axis the bleached interface roughened, indicating that microtubules slide past each

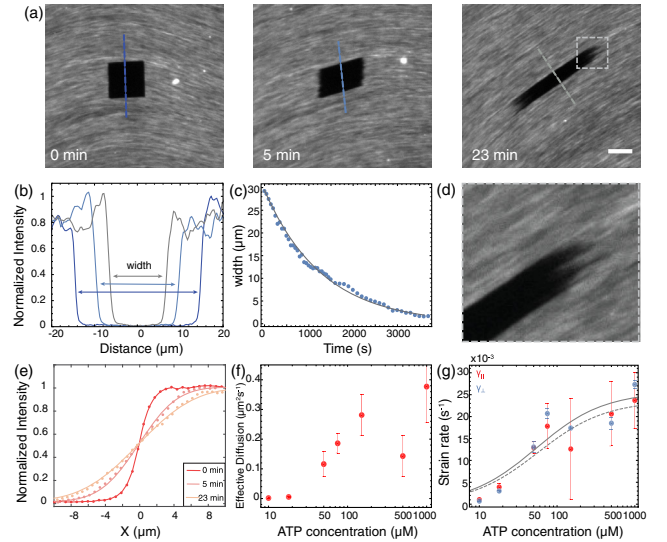


FIG. 2. Analysis of photobleached active nematics. (a) Time evolution of a photobleached region within a nematic assembled at $10 \mu\text{M}$ ATP. Scale bar, $20 \mu\text{m}$. (b) Intensity profiles I_{\perp} along the dotted lines in (a) and averaged across the length of the photobleached region. (c) The width of the photobleached region plotted over time, fitted to $w = ae^{-t/\tau}$. (d) Initially sharp, the edge of the bleached square along the director roughens over time. (e) Intensity profiles $I_{\parallel}(x)$ along the director averaged across the edge of the bleached region (points) and the prediction from the model of diffusion in Eq. (1) (lines). (f) The effective diffusion coefficient D_{bleach} extracted for Eq. (1) versus ATP concentration. (g) The strain rate as a function of ATP concentration. Strain rates extracted from the exponential fit $\gamma_{\perp} = 1/\tau$ (blue) and from a fit to the diffusion-convection model Eq. (1) (red). The gray lines are fits to the Michaelis-Menten equation $\gamma = \gamma_{\text{max}} [\text{ATP}] / (K_{\text{M}} - [\text{ATP}])$ with $\gamma_{\perp, \text{max}} = 0.026 \text{ s}^{-1}$ and $K_{\perp, \text{M}} = 54 \mu\text{M}$ (blue, dashed) and $\gamma_{\parallel, \text{max}} = 0.027 \text{ s}^{-1}$ and $K_{\parallel, \text{M}} = 46 \mu\text{M}$ (red, solid). Error bars in (f) and (g) are the standard errors of multiple measurements.

other collectively in staggered bundles [Fig. 2(d), Supplemental Material [38], Fig. S4]. This observation suggests the presence of complex spatiotemporal correlations in microtubule motions that remain poorly understood. Equation (1) separates the dynamics into extensile motion that drives the large-scale chaotic flows (γ_{\parallel}) and the stochastic contributions (D_{bleach}), by assuming that the microscopic motion of microtubules is the superposition of Gaussian random walk and spatially dependent drift processes. The similar ATP-dependent scaling of both γ and D_{bleach} suggests that both contributions are driven by the same microscopic processes.

To probe the origin of the stochastic contributions, we quantified the relative motions of individual filaments in active nematics by labeling a low fraction of microtubules [Fig. 3(a)]. We extracted relative velocities and orientations of labeled filament pairs using a custom MATLAB program [Fig. 3(b), Supplemental Material [38], movie 2]. To analyze only uniform domains, the relative velocities were calculated only for filament pairs aligned to within 10° . Averaging over all pairs yielded $V(x, y)$, which describes how the relative velocity of two microtubules depends on their separation along the x and y axis [Fig. 3(c)]. As previously, the microtubule's long axis defined the x axis in

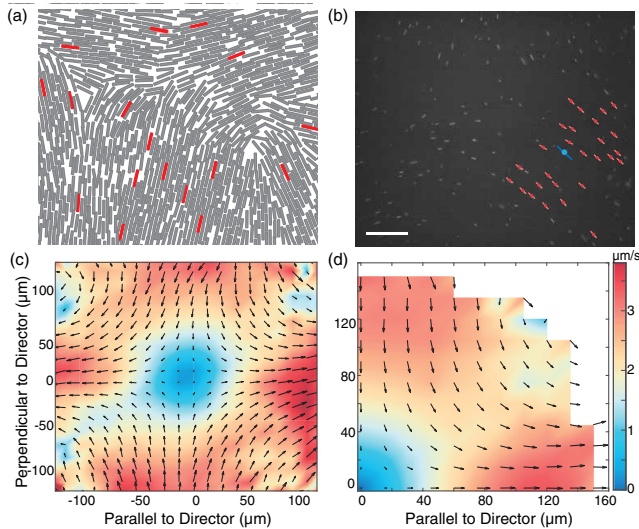


FIG. 3. Tracking microtubules in active nematics. (a) An active nematic doped with fluorescent microtubules. (b) An image of dilute fluorescent microtubules. The position (dot) and orientation (bar) of an example reference microtubule is overlaid in blue, and the aligned microtubules for which the relative velocities are calculated are plotted in red. One out of twenty-thousand microtubules is labeled. Scale bar, $25 \mu\text{m}$. (c) The average Lagrangian flow field in the reference frame of a microtubule located at the origin and oriented along x . The flow field was obtained from binning the relative velocities by distance and averaging over time and filament pairs ($1000 \mu\text{M}$ ATP). (d) The average flow field with relative microtubule positions and velocities collapsed into the first quadrant, so that $V_{\parallel} > 0$ indicates an extending pair.

the Lagrangian reference frame [Fig. 3(c)]. The velocities were broken into components along, $V_{\parallel}(x, y)$, and perpendicular to, $V_{\perp}(x, y)$, the nematic director. Exploiting the nematic symmetry, we collapsed the flow field by rotating microtubule pairs so that the nonorigin microtubule position was in the first quadrant [Fig. 3]. In this reference frame, $V_{\parallel} > 0$ indicates an extending pair, while $V_{\parallel} < 0$ indicates a contracting pair. Consistent with the photobleaching experiments, microtubule tracking also revealed dipolar extensile flows.

Plotting the velocity profiles along the x and y axis, $V_{\parallel}(x, 0)$ and $V_{\perp}(0, y)$, yielded relative filament velocities that, respectively, increased or decreased linearly with increasing filament separation [Figs. 4(a)–4(c)]. The slopes determined the ATP-dependent strain rates, which agreed with the photobleaching analysis [Fig. 5(a)]. Both photobleaching and filament tracking analysis revealed constant average strain rate and net dipolar extensile flows in the defect-free regions of the active nematic. A constant strain

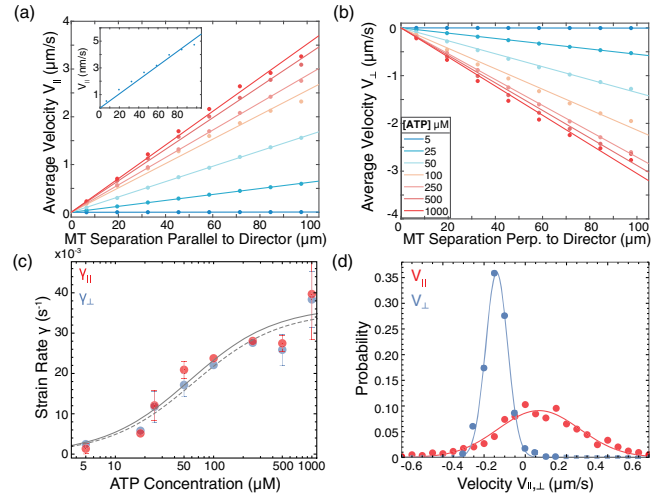


FIG. 4. Analysis of filament tracking data. (a) The average velocity of microtubule pairs along the director $V_{\parallel}(x, 0)$ as a function of interfilament distance along the director for all ATP concentrations [legend in panel (b)]. Inset: $5 \mu\text{M}$ velocity profile with a y -axis re-scaled to nm/s . (b) The average relative velocity perpendicular to the director $V_{\perp}(0, y)$ of microtubules as a function of the interfilament distance perpendicular to the director. (c) The strain rate calculated from the slope of the velocity profiles along the director (red) and perpendicular to the director (blue) plotted versus ATP concentration. The gray lines are fits of the data to the Michaelis-Menten equation with $\gamma_{\parallel, \text{max}} = 0.037 \text{ s}^{-1}$ and $K_{\parallel, \text{M}} = 57 \mu\text{M}$ (red, solid), and $\gamma_{\perp, \text{max}} = 0.035 \text{ s}^{-1}$ and $K_{\perp, \text{M}} = 63 \mu\text{M}$ (blue, dashed). Error bars are standard errors of multiple measurements. (d) The distribution of the microtubule sliding velocities for interfilament distance less than $6 \mu\text{m}$ ($50 \mu\text{M}$ ATP). Lines are fits of the data to Gaussians $P = A * e^{-(v-\bar{v})^2/2\sigma^2}$. Along the director (red), $\bar{v}_{\parallel} = 0.04$ and $\sigma_{\parallel} = 0.12 \mu\text{m/s}$. Perpendicular to the director (blue), $\bar{v}_{\perp} = -0.04$ and $\sigma_{\perp} = 0.07 \mu\text{m/s}$.

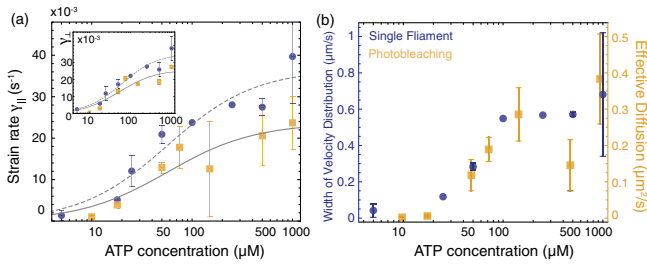


FIG. 5. Comparison of photobleaching and filament tracking results. (a) Strain rate along the director extracted from the slope of velocity profiles (blue dots) and Eq. (1) (gold squares). Inset: Strain rate perpendicular to the director from slope of velocity profiles (blue dots) and exponential fit of photobleached region width (gold squares). Gray lines are fits to the Michaelis-Menten equation. (b) Width of velocity distribution along the director σ_{\parallel} (blue dots, left axis) and effective diffusion coefficient D_{bleach} (gold squares, right axis) versus ATP concentration.

rate indicates exponential extension along the director. Similar dynamics were observed in growing bacterial colonies, although in that case the influx of mass yielded isotropic growth [46].

Tracking individual filaments not only revealed the average extension rate, but also the distribution of velocities around the average value. The probability distributions of the microtubule separation velocities along $p(V_{\parallel})$ and perpendicular to $p(V_{\perp})$ the director, showed the deviations of individual filaments from the average strain rate [Fig. 4 (d)]. Both distributions were Gaussians, with constant widths up to an interfilament distance of $30 \mu\text{m}$ (Supplemental Material [38], Fig. S5). Perpendicular to the director, the relative velocities were tightly distributed: all microtubules moved toward each other at comparable speeds, corresponding to the sharp intensity profiles (I_{\perp}) of the photobleached region [Figs. 2(a)–2(b)]. By contrast, velocities along the director deviated significantly from the average strain rate. On average, microtubule pairs moved away from each other. However, $p(V_{\parallel})$ had a significant contractile tail ($V_{\parallel} < 0$): at any given time $37\% \pm 2\%$ of microtubule pairs move toward each other.

We extracted the width of the velocity distribution σ_{\parallel} from a Gaussian fit to $p(V_{\parallel})$. Similar to the D_{bleach} measured in the photobleaching experiments, σ_{\parallel} reflects the stochastic contribution of the microtubule movements. Indeed, we found that both variables scaled similarly with ATP concentration [Fig. 5(b)]. For Brownian motion, the diffusion coefficient in the x direction is related to the width of the velocity distribution $D_{\text{single}} = \sigma_{\parallel}^2 \Delta t / 2$ [47]. However, we found that $D_{\text{single}} \neq D_{\text{bleach}}$ (Supplemental Material [38], Fig. S6). The assumption of Brownian dynamics behind D_{single} requires that particles act independently. In contrast, the jagged motion of microtubule bundles shows strong spatial correlations of microtubule motion [Fig. 2(d)]. Taken together, these observations

suggest that the underlying microscopic dynamics do not exhibit diffusion with Gaussian statistics.

Established models described active nematics by coarse-grained nematic director and velocity fields [8,9,12,15,48–51]. Such models capture certain features of the measured microtubule dynamics. Importantly, in a minimal model the local Lagrangian flows within a uniform domain exhibit relative extension speeds that grow linearly with distance (Supplemental Material [38], Fig. S7). This agreement shows that the coarse-grained behaviors of active nematics are generic and may be obtained from distinct microscopic dynamics. However, our experiments show that the dynamics of individual microtubules that create the net extensional flows exhibit nontrivial deviations from the mean velocity. This is a first step for informing the development of multiscale theories.

Our experiments revealed several features of active nematics. First, both stepping of isolated kinesin motors and the active nematic ATP-dependent strain rate are captured by the same Michaelis-Menten kinetic equations [26]. This demonstrates that the average extension rate is determined by the kinesin stepping speed. Second, the strain rate of an isolated filament pair is estimated by dividing the extension velocity [Fig. 1(b)] by the average microtubule length in the nematic, $\sim 2.5 \mu\text{m}$. This microscopic strain rate ($\sim 0.2 \text{ s}^{-1}$) is significantly larger than the effective strain rate measured in active nematics (0.03 s^{-1}) where multimotor and multifilament interactions are present (Supplemental Material [38], Fig. S8). This discrepancy suggests that the motors in dense nematics have different dynamics than those in the dilute solutions. One possibility is that motors in dense nematics experience high force loads, which reduces their stepping speed. Indeed, recent measurements suggested that the force load on kinesin is $\sim 20 \text{ pN}$ which generates significant prestress [52]. Third, given the nearly uniform extension rate of isolated bundles, one might also expect uniform extension in the active nematic, wherein all microtubules slide past each other at the same rate [30]. However, the measured distribution width of sliding velocities in dense nematics ($\sigma = 680 \text{ nm/s}$) is much larger than what is found for dilute bundles ($\sigma = 100 \text{ nm/s}$). Finally, the narrow distribution of velocities perpendicular to the director $p(V_{\perp})$ is consistent with active stress being generated only along the director. The movement of microtubules perpendicular to the director is driven by incompressible material flows, with the contraction rate along y reflecting the average extension rate along x .

The microscopic origin of the extensile or contractile symmetry breaking remains an open question. Numerical and theoretical work suggests that nonuniform motor distributions along filaments could be the microscopic source of the symmetry breaking, but these distributions are challenging to measure [53–55]. The measured filament velocity distributions provide an alternative parameter that

can perhaps be used to confirm specific microscopic models.

The microtubule velocity distributions determine the temporal evolution of a photobleached region. Uniform sliding velocities yield a photobleached area that splits into two distinct regions moving in the opposite directions, associated with opposing microtubule polarity [30]. Such dynamics were observed in 3D aligned microtubule gels powered by kinesin-14; all the microtubules moved at the same speed, exhibiting uniform extension that was identical to the isolated speed of the kinesin-14 motors [18]. In contrast, 2D active nematics exhibit nonuniform displacement along the edge of the bleached region. This striking difference suggests the existence of multiple classes of microscopic dynamics. Understanding the differences between these systems and their emergent dynamics is essential for developing accurate multiscale theories of active systems.

Importantly, in our experiments the edge of the photobleached region along the director does not blur smoothly; rather it roughens as discrete “bundles” of bleached and fluorescent microtubules slide past each other (Supplemental Material [38], Fig. S4, and movies 3, 4). This suggests that on short timescales bundles of microtubules move as cohesive units. One possibility is that the coherently moving regions have localized transient polar order [17,30], a hypothesis which could be verified with second harmonic generation microscopy [18,56].

In conclusion, we probed the dynamics of microtubules within dense 2D active nematics. The average flows are dipolar extensile with well-defined average strain rates. The microscopic motions are widely distributed about this average and cannot be captured by coarse-grained variables. The velocity distribution along the director and the appearance of coherent bundle motion implies that non-additive motor-microtubule interactions are important for generating extensile active stress.

This manuscript was primarily supported by the Department of Energy Basic Energy Science through Award No. DE-SC0019733 (L. M. L., S. J. D., and Z. D.). M. F. H. and S. F. acknowledges support from NSF DMR-1855914 and the Brandeis Center for Bioinspired Soft Materials, an NSF MRSEC (DMR-1420382 and DMR-2011846). A. M. T. is a Simons Foundation Fellow of the Life Sciences Research Foundation and is an Awardee of the Weizmann Institute of Science National Postdoctoral Award Program for Advancing Women in Science. We also acknowledge computational support from NSF XSEDE computing resources allocation TG-MCB090163 (Stampede) and the Brandeis HPC which is partially supported by DMR-1420382. We also acknowledge the KITP Active20 program, which is supported in part by the National Science Foundation under Grant No. NSF PHY-1748958.

- *zdogic@physics.ucsb.edu
- [1] M. C. Marchetti, J. F. Joanny, S. Ramaswamy, T. B. Liverpool, J. Prost, M. Rao, and R. A. Simha, Hydrodynamics of soft active matter, *Rev. Mod. Phys.* **85**, 1143 (2013).
 - [2] V. Narayan, S. Ramaswamy, and N. Menon, Long-lived giant number fluctuations in a swarming granular nematic, *Science* **317**, 105 (2007).
 - [3] S. Zhou, A. Sokolov, O. D. Lavrentovich, and I. S. Aranson, Living liquid crystals, *Proc. Natl. Acad. Sci. U.S.A.* **111**, 1265 (2014).
 - [4] T. B. Saw, A. Doostmohammadi, V. Nier, L. Kocgozlu, S. Thampi, Y. Toyama, P. Marcq, C. T. Lim, J. M. Yeomans, and B. Ladoux, Topological defects in epithelia govern cell death and extrusion, *Nature (London)* **544**, 212 (2017).
 - [5] K. Kawaguchi, R. Kageyama, and M. Sano, Topological defects control collective dynamics in neural progenitor cell cultures, *Nature (London)* **545**, 327 (2017).
 - [6] X.-q. Shi and Y.-q. Ma, Topological structure dynamics revealing collective evolution in active nematics, *Nat. Commun.* **4**, 3013 (2013).
 - [7] S. P. Thampi, R. Golestanian, and J. M. Yeomans, Instabilities and topological defects in active nematics, *Europhys. Lett.* **105**, 18001 (2014).
 - [8] L. Giomi, M. J. Bowick, X. Ma, and M. C. Marchetti, Defect Annihilation and Proliferation in Active Nematics, *Phys. Rev. Lett.* **110**, 228101 (2013).
 - [9] S. Shankar, S. Ramaswamy, M. C. Marchetti, and M. J. Bowick, Defect Unbinding in Active Nematics, *Phys. Rev. Lett.* **121**, 108002 (2018).
 - [10] E. Putzig, G. S. Redner, A. Baskaran, and A. Baskaran, Instabilities, defects, and defect ordering in an overdamped active nematic, *Soft Matter* **12**, 3854 (2016).
 - [11] A. U. Oza and J. Dunkel, Antipolar ordering of topological defects in active liquid crystals, *New J. Phys.* **18**, 093006 (2016).
 - [12] S. J. DeCamp, G. S. Redner, A. Baskaran, M. F. Hagan, and Z. Dogic, Orientational order of motile defects in active nematics, *Nat. Mater.* **14**, 1110 (2015).
 - [13] P. Guillamat, J. Ignés-Mullol, and F. Sagués, Taming active turbulence with patterned soft interfaces, *Nat. Commun.* **8**, 564 (2017).
 - [14] N. Kumar, R. Zhang, J. J. de Pablo, and M. L. Gardel, Tunable structure and dynamics of active liquid crystals, *Sci. Adv.* **4**, eaat7779 (2018).
 - [15] L. M. Lemma, S. J. DeCamp, Z. You, L. Giomi, and Z. Dogic, Statistical properties of autonomous flows in 2d active nematics, *Soft Matter* **15**, 3264 (2019).
 - [16] A. J. Tan, E. Roberts, S. A. Smith, U. A. Olvera, J. Arteaga, S. Fortini, K. A. Mitchell, and L. S. Hirst, Topological chaos in active nematics, *Nat. Phys.* **15**, 1033 (2019).
 - [17] M. J. Shelley, The dynamics of microtubule/motor-protein assemblies in biology and physics, *Annu. Rev. Fluid Mech.* **48**, 487 (2016).
 - [18] S. Fürthauer, B. Lemma, P. J. Foster, S. C. Ems-McClung, C.-H. Yu, C. E. Walczak, Z. Dogic, D. J. Needleman, and M. J. Shelley, Self-straining of actively crosslinked microtubule networks, *Nat. Phys.* **15**, 1295 (2019).
 - [19] K. Kruse and F. Jülicher, Actively Contracting Bundles of Polar Filaments, *Phys. Rev. Lett.* **85**, 1778 (2000).

- [20] F. Nédélec and T. Surrey, Dynamics of microtubule aster formation by motor complexes, *C. R. Acad. Sci.* **2**, 841 (2001).
- [21] M. Lenz, T. Thoresen, M. L. Gardel, and A. R. Dinner, Contractile Units in Disordered Actomyosin Bundles Arise from F-Actin Buckling, *Phys. Rev. Lett.* **108**, 238107 (2012).
- [22] D. Needleman and Z. Dogic, Active matter at the interface between materials science and cell biology, *Nat. Rev. Mater.* **2**, 17048 (2017).
- [23] P. J. Foster, S. Furthauer, M. J. Shelley, and D. J. Needleman, Active contraction of microtubule networks, *eLife* **4**, e10837 (2015).
- [24] J. Howard, A. J. Hudspeth, and R. D. Vale, Movement of microtubules by single kinesin molecules, *Nature (London)* **342**, 154 (1989).
- [25] K. Svoboda, C. F. Schmidt, B. J. Schnapp, and S. M. Block, Direct observation of kinesin stepping by optical trapping interferometry, *Nature (London)* **365**, 721 (1993).
- [26] K. Visscher, M. J. Schnitzer, and S. M. Block, Single kinesin molecules studied with a molecular force clamp, *Nature (London)* **400**, 184 (1999).
- [27] P. Bieling, I. A. Telley, J. Piehler, and T. Surrey, Processive kinesins require loose mechanical coupling for efficient collective motility, *EMBO Rep.* **9**, 1121 (2008).
- [28] H. Khataee and J. Howard, Force Generated by Two Kinesin Motors Depends on the Load Direction and Intermolecular Coupling, *Phys. Rev. Lett.* **122**, 188101 (2019).
- [29] K. Kruse, J. F. Joanny, F. Jülicher, J. Prost, and K. Sekimoto, Asters, Vortices, and Rotating Spirals in Active Gels of Polar Filaments, *Phys. Rev. Lett.* **92**, 078101 (2004).
- [30] T. Gao, R. Blackwell, M. A. Glaser, M. D. Betterton, and M. J. Shelley, Multiscale Polar Theory of Microtubule and Motor-Protein Assemblies, *Phys. Rev. Lett.* **114**, 048101 (2015).
- [31] R. Blackwell, O. Sweezy-Schindler, C. Baldwin, L. E. Hough, M. A. Glaser, and M. D. Betterton, Microscopic origins of anisotropic active stress in motor-driven nematic liquid crystals, *Soft Matter* **12**, 2676 (2016).
- [32] M. Striebel, I. R. Graf, and E. Frey, A mechanistic view of collective filament motion in active nematic networks, *Biophys. J.* **118**, 313 (2020).
- [33] F. Hilitski, A. R. Ward, L. Cajamarca, M. F. Hagan, G. M. Grason, and Z. Dogic, Measuring Cohesion between Macromolecular Filaments One Pair at a Time: Depletion-Induced Microtubule Bundling, *Phys. Rev. Lett.* **114**, 138102 (2015).
- [34] T. Sanchez, D. T. N. Chen, S. J. DeCamp, M. Heymann, and Z. Dogic, Spontaneous motion in hierarchically assembled active matter, *Nature (London)* **491**, 431 (2012).
- [35] G. Henkin, S. J. DeCamp, D. T. N. Chen, T. Sanchez, and Z. Dogic, Tunable dynamics of microtubule-based active isotropic gels, *Phil. Trans. R. Soc. A* **372**, 20140142 (2014).
- [36] P. Chandrakar, J. Berezney, B. Lemma, B. Hishamunda, A. Berry, K.-T. Wu, R. Subramanian, J. Chung, D. Needleman, J. Gelles, and Z. Dogic, Microtubule-based active fluids with improved lifetime, temporal stability and miscibility with passive soft materials, [arXiv:1811.05026](https://arxiv.org/abs/1811.05026).
- [37] G. Duclos, R. Adkins, D. Banerjee, M. S. E. Peterson, M. Varghese, I. Kolvin, A. Baskaran, R. A. Pelcovits, T. R. Powers, A. Baskaran, F. Toschi, M. F. Hagan, S. J. Streichan, V. Vitelli, D. A. Beller, and Z. Dogic, Topological structure and dynamics of three-dimensional active nematics, *Science* **367**, 1120 (2020).
- [38] See Supplemental Material at <http://link.aps.org/supplemental/10.1103/PhysRevLett.127.148001> for detailed experimental and analysis methods, and theoretical description, which includes Refs. [39–43].
- [39] R. Subramanian and J. Gelles, Two distinct modes of processive kinesin movement in mixtures of ATP and AMP-PNP, *J. Gen. Physiol.* **130**, 445 (2007).
- [40] M. Castoldi and A. V. Popov, Purification of brain tubulin through two cycles of polymerization–depolymerization in a high-molarity buffer, *Protein Expression Purif.* **32**, 83 (2003).
- [41] A. Hyman, D. Drechsel, D. Kellogg, S. Salser, K. Sawin, P. Steffen, L. Wordeman, and T. Mitchison, Preparation of modified tubulins, in *Molecular Motors and the Cytoskeleton*, Methods in Enzymology Vol. 196 (Academic Press, New York, 1991), pp. 478–485.
- [42] A. W. C. Lau, A. Prasad, and Z. Dogic, Condensation of isolated semi-flexible filaments driven by depletion interactions, *Europhys. Lett.* **87**, 48006 (2009).
- [43] S. Berg, D. Kutra, T. Kroeger, C. N. Straehle, B. X. Kausler, C. Haubold, M. Schiegg, J. Ales, T. Beier, M. Rudy, K. Eren, J. I. Cervantes, B. Xu, F. Beuttenmueller, A. Wolny, C. Zhang, U. Koethe, F. A. Hamprecht, and A. Kreshuk, ilastik: Interactive machine learning for (bio)image analysis, *Nat. Methods* **16**, 1226 (2019).
- [44] E. Berliner, E. C. Young, K. Anderson, H. K. Mahtani, and J. Gelles, Failure of a single-headed kinesin to track parallel to microtubule protofilaments, *Nature (London)* **373**, 718 (1995).
- [45] A. Ward, F. Hilitski, W. Schwenger, D. Welch, A. W. C. Lau, V. Vitelli, L. Mahadevan, and Z. Dogic, Solid friction between soft filaments, *Nat. Mater.* **14**, 583 (2015).
- [46] D. Dell’Arciprete, M. L. Blow, A. T. Brown, F. D. C. Farrell, J. S. Lintuvuori, A. F. McVey, D. Marenduzzo, and W. C. K. Poon, A growing bacterial colony in two dimensions as an active nematic, *Nat. Commun.* **9**, 4190 (2018).
- [47] H. Qian, M. P. Sheetz, and E. L. Elson, Single particle tracking. Analysis of diffusion and flow in two-dimensional systems, *Biophys. J.* **60**, 910 (1991).
- [48] L. Giomi, Geometry and Topology of Turbulence in Active Nematics, *Phys. Rev. X* **5**, 031003 (2015).
- [49] B. Martínez-Prat, R. Alert, F. Meng, J. Ignés-Mullol, J.-F. Joanny, J. Casademunt, R. Golestanian, and F. Sagués, Scaling Regimes of Active Turbulence with External Dissipation, *Phys. Rev. X* **11**, 031065 (2021).
- [50] M. M. Norton, A. Baskaran, A. Opathalage, B. Langeslay, S. Fraden, A. Baskaran, and M. F. Hagan, Insensitivity of active nematic liquid crystal dynamics to topological constraints, *Phys. Rev. E* **97**, 012702 (2018).
- [51] A. Opathalage, M. M. Norton, M. P. N. Juniper, B. Langeslay, S. A. Aghvami, S. Fraden, and Z. Dogic, Self-organized dynamics and the transition to turbulence of

- confined active nematics, *Proc. Natl. Acad. Sci. U.S.A.* **116**, 4788 (2019).
- [52] A. M. Tayar, M. F. Hagan, and Z. Dogic, Active liquid crystals powered by force-sensing dna-motor clusters, *Proc. Natl. Acad. Sci. U.S.A.* **118**, e2102873118 (2021).
- [53] T. B. Liverpool and M. C. Marchetti, Bridging the microscopic and the hydrodynamic in active filament solutions, *Europhys. Lett.* **69**, 846 (2005).
- [54] J. M. Belmonte, M. Leptin, and F. Nédélec, A theory that predicts behaviors of disordered cytoskeletal networks, *Mol. Syst. Biol.* **13**, 941 (2017).
- [55] M. Lenz, Reversal of contractility as a signature of self-organization in cytoskeletal bundles, *eLife* **9**, e51751 (2020).
- [56] C.-H. Yu, N. Langowitz, H.-Y. Wu, J. Bruges, and D. Needleman, Measuring microtubule polarity in spindles with second-harmonic-generation microscopy, *Biophys. J.* **106**, 1578 (2014).